Climatological sensitivities of shallow-cumulus bulk entrainment in continental and oceanic locations

Daniel J. Kirshbaum*

Department of Atmospheric and Oceanic Sciences, McGill University, Montreal, Quebec

Katia Lamer

Department of Environmental and Climate Sciences, Brookhaven National Laboratory, Upton, NY, USA

Corresponding author: Daniel Kirshbaum, daniel.kirshbaum@mcgill.ca

ABSTRACT

Cumulus entrainment is a complex process that has long challenged conceptual understanding and atmospheric prediction. To investigate this process observationally, two retrievals are used to generate multi-year climatologies of shallow-cumulus bulk entrainment (ϵ) at two Atmospheric Radiation Measurement cloud observatories, one in the US southern Great Plains (SGP) and the other in the Azores archipelago in the eastern North Atlantic (ENA). The statistical distributions of ϵ thus obtained, as well as certain environmental and cloud-related sensitivities of ϵ, are consistent with previous findings from large-eddy simulations. The retrieved ϵ robustly increases with cloud-layer relative humidity and decreases in wider clouds and cloud ensembles with larger cloud-base mass fluxes. While ϵ also correlates negatively with measures of cloud-layer vigor (e.g., maximum in-cloud vertical velocity and cloud depth), the extent to which these metrics actually regulate ϵ (or vice-versa) is unclear. Novel sensitivities of ϵ include a robust decrease of ϵ with increasing subcloud wind speed in oceanic flows, as well as a decrease of ϵ with increasing cloud-base mass flux in individual cumuli. A strong land–ocean contrast in ϵ is also found, with median values of 0.5-0.6 km^{-1} at the continental SGP site and and 1.0-1.1 km^{-1} at the oceanic ENA site. This trend is associated with drier and deeper cloud layers, along with larger cloud-base mass fluxes, at SGP, all of which favor reduced ϵ. The flow-dependence of retrieved ϵ implies that its various sensitivities should be accounted for in cumulus parameterization schemes.

1. Introduction

Cumulus entrainment and detrainment involve the ingestion of surrounding air, and the expulsion of cloudy air, through the periphery of cumulus clouds. These mixing processes regulate cloud mass fluxes and vertical transports, which, in turn, control the life cycle of moist convection and the interactions of this convection with the larger-scale environment. Due to the chaotic and turbulent nature of cloud mixing processes, the underlying dynamics of entrainment and detrainment, and hence the feedbacks of cumulus convection onto the larger scales, remain both poorly understood and inadequately represented in modern weather and climate models.

Although entrainment and detrainment are both critical to cloud life cycles, the focus herein is placed on entrainment due to its greater amenability to observational estimation. The primary impact of entrainment is to dilute ascending cloud drafts with drier and (generally) cooler air, which reduces cloud buoyancy and water content. As a result, entrainment can prevent cumuli from reaching their levels of neutral buoyancy (LNB) predicted by adiabatic parcel theory (e.g., Markowski and Richardson 2010). In some cases, entrainment can delay or even inhibit the diurnal transition from shallow to deep convection over land (e.g., Khairoutdinov and Randall 2006). Other, less obvious impacts of entrainment include a broadening of the cloud-droplet size spectrum, which may facilitate precipitation formation (e.g., Lasher-trapp et al. 2005).

Because entrainment influences cloud depth, phase (liquid vs ice), spatial coverage, and precipitation, it indirectly interacts with radiative processes controlling the global climate. The nature of these interactions remains uncertain in modern global climate models (GCMs), which cannot explicitly resolve most cumuli. Rather, they use cumulus parameterization schemes, which must make questionable assumptions about the entrainment (and detrainment) process, to represent the effects of moist convection on the resolved flow. Various studies have reported a strong sensitivity

of GCM simulations to the representation of cumulus entrainment (e.g., Rougier et al. 2009; Klocke et al. 2011; Dirmeyer et al. 2012), which reinforces the global importance of entrainment as well as the need to better constrain its magnitude.

Entrainment can be quantified in multiple ways, including "direct" methods that measure the mass flux across the cloud periphery (Romps 2010; Dawe and Austin 2011). Implementation of such methods requires full 3D wind fields and cloud boundaries at high spatiotemporal resolution, which in general are only available in large-eddy simulations (LES). In contrast, "bulk" methods measure not the entrainment itself but the impacts of entrainment on cloud dilution. Although exact calculation of bulk entrainment also requires 3D kinematic and thermodynamic data (Siebesma and Cuijpers 1995), the widely used "bulk-plume" simplification of Betts (1975) requires only a representative sounding and in-cloud measurements of a moist conserved variable. Because only bulk calculations are currently feasible observationally, only these methods are considered herein. Emphasis will be placed on quantifying the fractional entrainment (or dilution) rate $\epsilon = E/M_c$, where E is the total entrainment flux and M_c is the cloud vertical mass flux.

Much of the current understanding of ϵ is based on cloud-resolving simulations (including LES), which simulate cumuli at sufficient spatiotemporal resolution to partially resolve entrainment. LES studies examining the relation between ϵ and corresponding kinematic/thermodynamic cloud properties have indicated that simulated ϵ roughly varies with cloud-averaged w^{-1} or b/w^2, where w and b are vertical velocity and buoyancy (e.g., Gregory 2001; Neggers et al. 2002; Tian and Kuang 2016; Zhang et al. 2016).

Bulk entrainment also tends to decrease with increasing cloud cross-sectional area (e.g., McCarthy 1974; Kirshbaum and Grant 2012; Rieck et al. 2014), likely because larger clouds are less diluted by a given entrainment flux across the cloud periphery than smaller clouds. It also tends to decrease with increasing subcloud- and cloud-layer depths (e.g., Del Genio and Wu 2010; Stirling

and Stratton 2012; Drueke et al. 2020), consistent with both energetic (Grant and Brown 1999) and cloud-morphological arguments. In isotropic turbulence, the largest energy-containing eddies tend to scale with the layer depth, implying that deeper subcloud or cloud layers support wider, and hence less diluted, cumuli.

Environmental conditions also play a role in governing ϵ. Although some debate on the impact of cloud-layer humidity ($\mathrm{RH_{cld}}$) has prevailed over the years, the emerging LES-based consensus is that ϵ increases strongly and robustly with $\mathrm{RH_{cld}}$ (Stirling and Stratton 2012; Bera and Prabha 2019; Drueke et al. 2020). This trend can be explained by a buoyancy-sorting argument: in drier layers, mixtures of cloud and surrounding air are more prone to buoyancy reversal, leading them to detrain rather than entrain. Similar logic may explain the tendency for ϵ to increase with convective available potential energy (CAPE) (Stirling and Stratton 2012): in smaller-CAPE flows, less cloud buoyancy is generated, and cloud–environmental mixtures are more likely to lose buoyancy and detrain.

The background wind profile may also be expected to influence ϵ, but its impacts remain unclear. In particular, cloud-layer vertical shear (S_{cld}) may influence ϵ through its dynamical impacts on moist thermals. In shear flows, ascending thermals develop cloud-scale horizontal circulations with strong inflow on the downshear side, which locally enhances ϵ (e.g., Heymsfield et al. 1978). However, shear has also been found to increase cloud width, which tends to decrease ϵ (Peters et al. 2019). These competing effects may help to explain a wide variation in ϵ–S_{cld} trends reported in past studies (e.g., Brown 1999; Peters et al. 2019; Drueke et al. 2019a; Yamaguchi et al. 2019).

Interestingly, Drueke et al. (2020) identified a strong land–ocean contrast in ϵ; its value over land was less than half that over the ocean. They attributed this finding to stronger sensible heating over land, which energizes subcloud turbulence and increases the cloud-base mass flux (m_b). Although

the total cloud entrainment flux (E) increases in response, it cannot keep pace with m_b because it is also constrained by CAPE, leading to decreased ϵ (Kirshbaum and Grant 2012).

Although numerical simulations, and LES in particular, offer an attractive avenue for studying cumulus entrainment, results from these models are inherently uncertain and should be verified observationally. Observations are also valuable for sampling a wider range of cumulus environments than is possible with LES. However, observational estimation of entrainment remains in its infancy. Only bulk estimates are currently feasible, and these have their own set of challenges. The most reliable ϵ estimates arguably come from aircraft, which can provide in situ observations within cloud transects at different heights, from which ϵ can be retrieved using the bulk-plume method (e.g., Raga et al. 1989; Gerber et al. 2008). Even so, aircraft cloud sampling is limited by large costs and the practical difficulties of safely maneuvering through cloud fields.

Much greater sampling of cumuli is possible with remote measurements. Unlike research aircraft, however, these instruments do not readily provide detailed thermodynamic information within clouds, and thus a greater level of approximation is required to estimate ϵ. Using satellite estimates of cloud-top height and temperature, Luo et al. (2010) employed an entraining parcel model to estimate the mean ϵ over the cloud depth. Applying this method to multiple years of satellite data, Takahashi et al. (2017) found that deep convection over the west Pacific warm pool had smaller cloud widths and larger ϵ than that over two tropical land masses, consistent with the land–ocean ϵ contrast identified by Drueke et al. (2020) as well as the tendency for wider clouds to undergo less dilution.

The present study focuses on bulk entrainment within shallow cumuli (ShCu), which are globally widespread but difficult to represent in GCMs due to their small scales (e.g., Bony and Dufresne 2005). The Luo et al. (2010) retrieval cannot be used for ShCu because infrared satellites do not resolve them. However, such retrievals are possible at ground-based cloud observatories,

including US Department of Energy Atmospheric Radiation Measurement (ARM) sites. Jensen and Del Genio (2006, or JD06) used soundings and radar-derived cloud-top heights, along with an entraining parcel model, to estimate ϵ over the ARM-instrumented tropical island of Nauru. In 67 cumulus congestus clouds, ϵ was found to increase with both RH_{cld} and CAPE, consistent with the buoyancy-sorting arguments above. Other ground-based techniques to retrieve ϵ in ShCu include the sophisticated optimal-estimation method of Wagner et al. (2013) and the analytical method based on turbulent kinetic energy (TKE) similarity theory of Drueke et al. (2019b), neither of which has yet been deployed on a large set of observed clouds.

The current study capitalizes on roughly four years of observations collected at the ARM Southern Great Plains (SGP) and Eastern North Atlantic (ENA) facilities to (i) generate climatologies of ShCu bulk entrainment in continental and oceanic climates and (ii) determine the sensitivity of retrieved ϵ to various relevant parameters. To this end, section 2 describes our treatment of the ARM observations, and section 3 details two bulk entrainment retrieval methods used for the climatologies. Section 4 presents the climatologies and describes the various sensitivities of the retrieved ϵ. Section 5 discusses underlying mechanisms behind the observed sensitivities, as well as future directions for improvement of ground-based ϵ retrievals. Section 6 presents the conclusions.

For ease of reference, all mathematical symbols used herein are defined in Table 1.

2. Observations

Observations from two ARM observatories, the Southern Great Plains (SGP; 36.6N, 97.5W) and Eastern North Atlantic (ENA; 39.1N, 28.0W) sites, are used to evaluate the impact of continentality on midlatitude ShCu. The former, located in north-central Oklahoma, represents the continental regime and the latter, located in the Azores archipelago, represents the oceanic regime. Both

observatories are equipped with equivalent sets of ground-based remote sensors such that the same observational approach can be applied to both.

The observations are used to construct climatologies of ShCu ϵ at both sites using two different retrievals, the JD06 parcel-based calculation for individual clouds and the D19 TKE-based cloud-ensemble calculation. Details on these methods and their applicability is given in section 3. In this section, we define and outline the determination of various cloud-related and environmental properties involved in the retrieval of bulk entrainment. Additional properties are also estimated to evaluate their possible impact on bulk entrainment.

a. Remotely sensed properties

ShCu are known to be challenging observational targets. Their small horizontal footprint causes wide-beam sensors like microwave radiometers and spaceborne radars to misrepresent their properties, an issue known as partial beam filling (Lamer and Kollias 2015; Battaglia et al. 2020). Although ground-based radars benefit from a narrower beam width, detection issues persist because fair-weather cumuli tend to have small water contents and droplet sizes, making them poor reflectors of millimeter-radar signals (Lamer and Kollias 2015). Herein we exploit the synergy between a vertically pointing Ka-band ARM Zenith Radar (KAZR), micropulse lidar, ceilometer, microwave radiometer (MWR), and vertically pointing Doppler Lidar at ARM observatories to estimate the location and properties of shallow cumuli at 30-m vertical and 4-s temporal resolution. With the exception of the Doppler Lidar observations, these observations are contained within the ARM Active Remote Sensing of CLouds (ARSCL) product.

The ARSCL product provides a first estimate of the cloud location within the column in the form of a "cloud source flag". We have developed a set of additional filters designed specifically to reduce the possibility of fair-weather cumulus misdetection in the ARSCL product. These are

based on independent data from the Doppler Lidars, which are first filtered to remove noisy echoes with signal-to-noise ratios below 0.0075. The next filter targets any flagged clouds with maximum radar reflectivity below -45 dBZ if the Doppler Lidar did not also detect at least two coincident observations of attenuated backscatter $\gamma > \gamma_t = 2 \times 10^{-5}$ m^{-1}s^{-1} and if the microwave radiometer reported a liquid water path of at least 20 g m^{-2}. We also revise the ARSCL cloud-base-height estimates if the Doppler Lidar backscatter at that height is less than γ_t while the maximum Doppler Lidar backscatter in the cloudy column exceeds γ_t. In those instances, revising the column cloud-base-height to be the lowest level at which the backscatter exceeds γ_t yields improved agreement with radar-observed cloud-base height.

Using the revised ARSCL cloud source flag, we define an individual cloud as a distinct and connected (based on a four-neighbor routine) set of cloud observations in time-height space and a cloud ensemble as a group of individual clouds observed during a given 1-h time period. Although this short time window limits the number of cloud observations within each ensemble, it helps to limit the degree of larger-scale and diurnal variability during each cloudy period, so that a representative environment can be defined. Using the ARSCL and Doppler Lidar observations, the following quantities are computed:

1. Cloud duration (t_{cld}): Time elapsed between the first and last detection of a given cloud. Only defined for individual clouds.

2. Radar-observed cloud cover ($\mathrm{CCF}_{\mathrm{rad}}$): Fraction of radar-observed cloudy columns in an hourlong cumulus period. Only defined for cloud ensembles.

3. Minimum cloud base height (z_b): 2nd percentile of revised column cloud-base-height estimate within the time limits of each individual cloud or cumulus ensemble.

4. Maximum cloud top height (z_t): 98th percentile of column cloud-top heights within the time limits of each individual cloud or cumulus ensemble.

5. Maximum cloud layer depth (d_{cld}): $z_t - z_b$. Note that this calculation may underestimate the true cloud depth when the tallest part of a given cloud, or the tallest cloud of a given cumulus ensemble, does not pass over the observatory.

6. Cloud maximum updraft speed (w_{max}): Maximum KAZR Doppler velocity over a given cloud (JD06) or over all clouds in a cumulus ensemble (D19).

7. Maximum liquid-water path ($\mathrm{LWP}_{\mathrm{max}}$): Maximum MWR-observed LWP over a given cloud (JD06) or over all clouds in a cumulus ensemble (D19).

8. Subcloud vertical velocity variance ($\left(\sigma_w^2\right)_{\mathrm{sc}}$): Vertical velocity variance between the surface and z_b over the hourlong period centered at the temporal midpoint of the individual cloud or cumulus ensemble.

b. Sounding-derived properties

Because both retrievals are highly sensitive to atmospheric thermodynamics, special care is taken to construct a representative sounding at any desired time. Sources of thermodynamic data include balloon radiosondes, launched at 3 h to 12 h intervals and interpolated to the time of interest, European Centre for Medium-Range Weather Forecasting Diagnostic Analyses interpolated to the SGP site (ECMWF-DIAG; ARM data stream "ecmwfvar"), and hourly-averaged water-vapor mixing ratio profiles from Raman Lidar, centered at the time-midpoint of the cloud or cloudy period with a vertical resolution of 7.5 m. Because the ECMWF analyses and Raman Lidar profiles cover a larger time scale than that of individual clouds, they are likely to better represent the cloud environment than the more instantaneous balloon soundings.

To ensure that the sounding reasonably represents the cloud environment, we construct four different candidate soundings for each retrieval: (i) time-interpolated radiosonde, (ii) ECMWF analysis, and (iii)-(iv) modified versions of (i) and (ii) where the low-level water-vapor mixing ratio is replaced by corresponding Raman Lidar data. An adiabatic air parcel ascent, initialized from mean-layer (0-500 m) properties, is conducted for each sounding to determine the lifting condensation level (LCL), level of free convection (LFC), and level of neutral buoyancy (LNB). The LFC and LNB are respectively defined as the lowest and highest levels above the LCL where the parcel buoyancy b is positive, where $b = g(T_{vp} - T_{ve})/T_{ve}$ and T_{vp} and T_{ve} are the virtual temperatures of the parcel and environment. Of these four profiles, the one with its LCL nearest to the observed cloud base is taken to be most representative. The various properties computed from this sounding include

1. Convective available potential energy (CAPE): Vertically integrated b between the LFC and the LNB.

2. Cloud-layer CAPE (CAPE_{cld}): Vertically integrated b between the LFC and z_t.

3. Convective Inhibition (CIN): Vertically integrated $|b|$ between the surface and the LFC.

4. Cloud-layer-averaged relative humidity (RH_{cld}): Vertically averaged relative humidity (with respect to liquid) between z_b and z_t.

5. Cloud-layer-averaged vertical shear (S_{cld}): Magnitude of vertically averaged (between z_b and z_t) vertical wind shear.

6. Subcloud-layer-averaged wind speed (V_{sc}): Magnitude of vertically averaged (between surface and z_b) wind velocity.

7. Cloud-layer-averaged mean wind speed ($V_{\rm cld}$): Magnitude of vertically averaged (between z_b and z_t) horizontal wind vector.

8. Cloud width ($L_{\rm cld}$): Given by $V_{\rm cld}t_{\rm cld}$, and only defined for individual clouds. Because $t_{\rm cld}$ includes overhanging edges of vertically tilted clouds, $L_{\rm cld}$ may be enhanced by such tilt. Moreover, because this estimate assumes that clouds are advected by the mean cloud-bearing-layer wind, it is prone to error in cases where cloud motion is governed by other processes.

9. Cloud-base mass flux (M_b and m_b): For individual clouds, M_b (in kg m^{-1} s^{-1}) represents the total cloud upward mass flux over the cloud duration, and is evaluated as

$$M_b = \rho_b L_{\rm up} w_{\rm up}\,, \tag{1}$$

where $L_{\rm up} = V_{\rm cld}t_{\rm up}$ is the width of the cloud-base updraft(s), $t_{\rm up}$ and $w_{\rm up}$ are the time duration and mean ascent rate of the cloud-base updraft, and $\rho_{\rm b}$ is the cloud-base density. For cumulus ensembles, the density-normalized cloud-base mass flux m_b (in m s^{-1}) is

$$m_b = f_{\rm up} w_{\rm up}\,, \tag{2}$$

where $f_{\rm up}$ is the fractional coverage of ascending cloud-base cloudy points during the hourlong period (Grant and Lock 2004).

c. Sensible heat flux

An additional parameter of interest is surface sensible heat flux H, which may regulate ϵ through its control over m_b (Drueke et al. 2020). This quantity is obtained at 30-min intervals from the ARM Eddy Covariance Flux Measurement System (ECOR), which uses quality control procedures to modify the raw eddy covariances to better close the surface energy balance. Because H may exhibit substantial small-scale variability (particularly over heterogeneous surfaces), such point

measurements may not represent the averaged surface heating over the cloud life cycle (Zhang and Klein 2010).

3. Bulk entrainment retrievals

The two retrieval methods used herein were selected based on the LES Observation System Simulation Experiments (OSSEs) of D19, where different pseudo-retrievals of ϵ were systematically compared to corresponding model calculations of ϵ. In their evaluation, the JD06 and D19 methods exhibited much smaller mean absolute errors in ϵ (20-30%) than that of Wagner et al. (2013) (50%). Although both the JD06 and D19 methods invoke assumptions that may limit their accuracy and applicability (see section 3 for details), the use of multiple retrievals helps to identify robust statistical trends despite these limitations.

a. The JD06 method for individual clouds

This approach, adapted from JD06, uses an entraining-parcel model to estimate the ϵ experienced by individual, surface-based cumuli that breach the LFC. We implement this method on selected clouds using the observations discussed above, by drawing a mean-layer parcel from the representative sounding and lifting it adiabatically to the LFC. Above the LFC, the parcel entrains environmental air at a constant rate ϵ until reaching its entraining level of neutral buoyancy (ELNB). Bulk entrainment (ϵ_{JD06}) is retrieved by iteratively varying ϵ until the parcel ELNB best matches the observed z_t. Note that we use T_v as a buoyancy variable in place of equivalent potential temperature θ_e (as was done in JD06) to account for virtual effects, which tends to give a slightly deeper active (buoyant) cloud layer and an associated reduction in retrieved bulk entrainment.

Several assumptions are made in this retrieval, one being that entrainment is lateral and homogeneous; entrained air is drawn from the environment at the same height as the parcel and mixes

instantaneously through the parcel. It also assumes that the observed cloud top is neutrally buoyant, which is problematic in growing clouds where cloud-top buoyancy drives continued ascent. Although this assumption tends to generate systematic positive biases in ϵ_{JD06}, Drueke et al. (2019b) found that the bias could be partly mitigated by setting a minimum cloud depth threshold (250 m). This threshold helped to filter out newly initiated and rapidly growing cumuli that most strongly violate the assumption of zero cloud-top buoyancy. Nevertheless, a bias toward overly strong ϵ is likely to persist for all remaining clouds that continue to grow after crossing the radar site.

Another key assumption is a vertically constant ϵ over the cloud layer, which contrasts with the tendency for simulated and observed ϵ in ShCu to decrease with height (e.g., Brown et al. 2002; Siebesma et al. 2003; Gerber et al. 2008). JD06 considered this issue by comparing a fixed ϵ profile to one that depended inversely on b, but did not find any major differences in the retrieved values or sensitivities of ϵ in ShCu. On that basis, we have opted not to include this effect.

b. The D19 method for cloud ensembles

D19 proposed a method to estimate the bulk entrainment based on a similarity theory of shallow-cumulus transports developed by Grant and Brown (1999). This theory is based on the assumption that buoyancy production ($\sim m_b \mathrm{CAPE}/d_{\mathrm{cld}}$) and dissipation ($\sim {w^*}^3/d_{\mathrm{cld}}$, where w^* is the turbulent vertical velocity scale) dominate the steady-state cloud-layer TKE budget, which gives $w^* = (m_b \mathrm{CAPE})^{1/3}$. Assuming that $E \sim \epsilon m_b {w^*}^2$ scales with these dominant terms, $\epsilon \sim \mathrm{CAPE}/d_{\mathrm{cld}} {w^*}^2$, or equivalently,

$$\epsilon_{\mathrm{D19}} = A_\epsilon \frac{{\mathrm{CAPE}_{\mathrm{cld}}}^{1/3}}{m_b^{2/3} d_{\mathrm{cld}}}, \tag{3}$$

where A_ϵ is a constant representing the fraction of buoyancy production available for entrainment, with previously reported values ranging from 0.03-0.06 (Grant and Brown 1999; Kirshbaum and Grant 2012; Drueke et al. 2019b). We implement this method on the above-mentioned observations,

selecting $A_\epsilon = 0.06$ to maximize empirical agreement with the JD06 results. While this choice affects the absolute values of ϵ_{D19}, it has no impact on the associated sensitivities.

To provide some physical insight into (3), we note that dependence of ϵ on d_{cld}^{-1} (for all else being equal) is owing to amplified cloud-layer energetics when the cloud buoyancy production is confined to a shallower layer. The sensitivities to CAPE and m_b can also be interpreted in energetic terms: CAPE/w^{*2} effectively represents the efficiency of conversion from subcloud available potential energy to cloud-layer kinetic energy. A larger ratio implies a smaller conversion efficiency, which is consistent with entrainment more strongly suppressing the cloud-layer updrafts.

Key assumptions of the D19 method include statistical stationarity, which is more applicable to long-lived oceanic cumulus fields than to diurnally forced ShCu over land. This assumption is tolerable if the cloud-layer turbulent adjustment time scale (i.e. the eddy turnover time) is much shorter than the diurnal or synoptic time scales, which is usually the case (Kirshbaum and Grant 2012). It also assumes that cloud buoyancy production is the dominant TKE source term, which does not necessarily hold in strongly sheared flows. Thus, D19 is most applicable to statistically steady, nonprecipitating, and unsheared ShCu fields. Nevertheless, it will be applied to all cloud ensembles that satisfy similar eligibility criteria to the JD06 method, regardless of their degree of steadiness or shear.

c. Case selection based on retrieval limitations

The ShCu bulk-entrainment climatologies presented herein cover a 4+ yr period (10 November 2015 to 19 December 2019), over which many ShCu clouds and cloud ensembles were observed at both ARM sites. However, due to the various assumptions behind each retrieval, as well as inherent difficulties in observing ShCu via ground-based radars, the number of clouds for which entrainment is actually retrieved is much less. To respect the assumptions of the two retrieval

methods, we focus on daytime (surface-based), nonprecipitating, and active (buoyant) fair-weather cumuli, which we identify using the following criteria.

1. Daytime criteria. Because both ARM sites are on land, nocturnal radiative cooling can cause the subcloud layer to decouple from the surface. As both retrievals apply to surface-based cumuli, we restrict consideration to daytimes (06:00-18:00 local solar time, or LST).

2. Observable criteria. To avoid misrepresentation of cloud-top height, clutter and insect-contaminated 1-h periods are removed following the method of Lamer and Kollias (2015).

3. Cumulus criteria. All 1-h periods with cloud tops below 5 km, $\mathrm{CCF_{rad}}$ between 6-60%, and no clouds lasting longer than 20 min are labeled as cumulus ensembles. A total of 477 (1,432) such ensembles were identified at SGP (ENA). On days containing one or more ensembles, all clouds below 5 km detected for more than 1 min but less than 20 minutes are labeled as individual cumuli. A total of 4,480 (18,877) such clouds were identified at SGP (ENA).

4. Active (i.e., buoyant and surface-based) cloud criteria. Both the JD06 and the D19 retrievals assume that entrainment is confined to the layer between the LFC and cloud top. Thus, only "active" clouds that breach the LFC are considered, which are identified by requiring that $\mathrm{CAPE_{cld}} > 0$, $z_t >$ LFC, and $[m_b, M_b] > 0$. Elevated clouds are also eliminated by filtering out clouds with $z_b > 3$ km or $z_b >$ LFC + 250 m, as well as cumulus ensembles with large (> 200 m) standard deviations of cloud-base height.

5. Neutrally buoyant cloud-top criteria. To mitigate the biases associated with the assumption of neutrally buoyant cloud tops in the JD06 retrieval, we follow Drueke et al. (2019b) by filtering out very shallow clouds with $d_{\mathrm{cld}} < 250$ m.

6. Nonprecipitating cloud criteria. The D19 and, to a lesser extent, the JD06 formulations apply more readily to nonprecipitating cumuli. To remove precipitating clouds, we eliminate clouds exhibiting an in-cloud maximum reflectivity exceeding −5 dBZ and the maximum reflectivity at 90 m below cloud base exceeding −20 dBZ.

7. Unrepresentative environment criteria. To avoid soundings that pass directly through clouds and are thus unrepresentative of the surrounding environment, retrievals are omitted when the sounding-derived $\mathrm{RH_{cld}}$ exceeds 99%.

8. Retrieval convergence. The JD06 retrieval uses an iterative loop to determine ϵ_{JD06}. If, at the end of the iterations, the absolute difference between the ELNB and z_t exceeds 500 m or $d_{\mathrm{cld}}/2$, the retrieval is omitted.

Application of the above criteria allow for the retrieval of bulk entrainment in 887 (3,724) individual clouds and 175 (631) cloud ensembles at SGP (ENA).

4. Bulk entrainment

In this section, we present the JD06 and D19 climatologies of ShCu bulk entrainment at SGP and ENA and analyze the sensitivities of the retrieved ϵ to environmental and cloud-related parameters.

a. The land–ocean contrast in ϵ

Probability density functions (PDFs) of bulk entrainment are shown for the JD06 and D19 retrievals in Fig. 1. At both SGP and ENA, the probability peaks at the smallest values ($\epsilon \leq 0.5$ km^{-1}), and generally declines with increasing ϵ. Because of its longer tail, the median ϵ_{JD06} at ENA (1.03 km^{-1}) exceeds that at SGP (0.62 km^{-1}) by approximately 66%. Similar findings are obtained with ϵ_{D19}, with the median value at ENA (1.06 km^{-1}) about 88% larger than that at SGP

($0.56\,\mathrm{km}^{-1}$). These median values for both continental and oceanic entrainment rates are consistent with previous LES and observational studies (e.g., Brown et al. 2002; Siebesma et al. 2003; Gerber et al. 2008; Drueke et al. 2020). Thus, both retrievals give a consistent and robust result that bulk entrainment is larger in the oceanic ENA climate than in the continental SGP climate.

The above finding is consistent with the LES experiments of Drueke et al. (2020), where ϵ in oceanic clouds was found to be much larger than that over land. However, their ratio of land to ocean entrainment (2.2) was slightly larger than found here (1.6-1.9). This weaker land–ocean entrainment contrast may stem from the fact that the ENA site, while surrounded by oceanic flow, is located on land and thus not fully representative of flow over the open ocean. The likely drivers of this land–ocean ϵ contrast will be discussed in section 5a.

b. Sensitivities of ϵ

The relationship between retrieved ϵ and various environmental parameters (causal or not) is assessed by evaluating statistics of ϵ within eight bins covering the observed ranges for each parameter (Figs. 2-5). In each bin, the 25th percentile, median, and 75th percentile of ϵ are shown. The presence of a statistically significant monotonic (but not necessarily linear) relation between the control parameter and the median ϵ is assessed based on the Spearman correlation p-value. For p-values below 0.05, the null hypothesis of no monotonic relation can be rejected at the 95% confidence level. If the relation is deemed "significant" by this metric, the line connecting the medians is drawn as solid; otherwise, the line is dashed. The strength of a given correlation is indicated by the Spearman correlation coefficient R.

1) Environmental parameters

Arguably the strongest and most robust sensitivity of ϵ is to RH_{cld}, with the median ϵ increasing from around 0.5 km^{-1} to over 1 km^{-1} as RH_{cld} increases from 50% to 100% (Figs. 2h and 3h). This positive trend is significant for both retrievals, with R ranging from 0.79 to unity, and is consistent with recent LES studies (Stirling and Stratton 2012; Drueke et al. 2020) as well as observations (JD06, Lamer et al. 2015; Lu et al. 2018). As noted in section 1, it may be explained by a greater tendency for cloud-environmental mixing to lead to buoyancy reversal, and hence detrainment (at the expense of entrainment), in drier cloud layers (Drueke et al. 2020).

A positive and strong correlation between ϵ and CAPE is found at ENA ($R \geq 0.88$), but this trend weakens and loses significance at SGP (Figs. 2a and 3a). Moreover, the correlation between ϵ and $CAPE_{cld}$ is weak at SGP and variable at ENA (Figs. 2b and 3b). These trends generally differ from the strong positive sensitivity of ϵ to low-level CAPE in JD06. However, because JD06 studied a single maritime location (the tropical island Nauru) and did not evaluate $CAPE_{cld}$, their results are most comparable to the CAPE trend at ENA in Fig. 2a, which is positive and statistically significant.

The generally stronger sensitivity of ϵ to CAPE than to $CAPE_{cld}$ may relate to our ShCu sampling criterion that $z_t \leq 5$ km. For moist-unstable layer (and CAPE) depths of 5 km and higher, the cumuli that satisfy this condition become increasingly diluted. If deeper clouds were also considered, their tendency to be less diluted would likely weaken this correlation. In contrast, $CAPE_{cld}$ is more representative of the cloud's immediate environment, but its estimates depend on cloud top height, and hence may capture other effects (some offsetting) that control ϵ.

A significant and strong ($R < -0.88$) negative sensitivity of ϵ to V_{sc} is found at ENA (Figs. 2e and 3e). Although this interesting relationship requires further investigation to properly interpret,

the tendency for stronger marine flows to generate deeper clouds (Nuijens and Stevens 2012), combined with the negative sensitivity of ϵ to d_{cld} (as will be shown shortly), provides a potential explanation. Also, the general insensitivity of ϵ to H in Figs. 2f and 3f disagrees with the hypothesis of Drueke et al. (2020) that larger H, by virtue of its control over m_b in (3), leads to reduced ϵ. This contradiction will be revisited in section 5a.

No clear correlations are found between ϵ and CIN (Figs. 2c and 3c) or S_{cld} (Figs. 2d and 3d). The latter contrasts with a strong positive trend in ϵ found in simulated trade-wind ShCu (Drueke et al. 2019a) as well as a negative trend found in simulated supercells (Peters et al. 2019). It is more in line with the weak relations between S_{cld} and ϵ reported by Brown (1999) and Yamaguchi et al. (2019), and suggests that multiple offsetting effects of S_{cld} may combine to yield minimal net ϵ sensitivity. Also, while ϵ tends to vary inversely with $\left(\sigma_w^2\right)_{\text{sc}}$ (Figs. 2g and 3g), this trend is neither robust nor statistically significant.

2) Cloud-related parameters

The retrieved ϵ varies more strongly with cloud-related parameters than with the above-mentioned environmental parameters. It varies inversely, and to varying degrees, with all measures of cloud vigor, including d_{cld} (Figs. 4b and 5b), LWP_{max} (Figs. 4c and 5c), and w_{max} (Figs. 4f and 5e). Of these relationships, the strongest is between ϵ and d_{cld}, which uniformly exhibits $R \leq -0.75$ but is not always statistically significant.

It is fair to question whether the above measures of cloud vigor causally control ϵ, are controlled by ϵ, or only correlate with ϵ due to cross-correlations with other controlling parameters. For example, while Neggers et al. (2002) considered w_{max} to be a controlling parameter for ϵ, Rousseau-Rizzi et al. (2017) argued that the relationship between these two variables was reversed. Similarly, although an inverse sensitivity of ϵ to d_{cld} is expected given (3), this trend may also stem in part

from the strong sensitivity of cloud vertical development to ϵ (e.g., Khairoutdinov and Randall 2006). Thus, the relationships between ϵ and the measures of cloud vigor ($w_{\max}$, $\mathrm{LWP}_{\max}$, and d_{cld}) are likely interactive and not a simple matter of one parameter controlling the other.

The two retrievals give inconsistent results on the relationship between z_b and ϵ (Figs. 4a and Figs. 5a). For this parameter, only one correlation proved statistically significant: a decrease in ϵ_{JD06} with increasing z_b in the continental SGP climate. While a similar, though not significant, negative trend is also found at ENA in both retrievals, the D19 retrieval indicates a weakly positive relationship between ϵ_{D19} and z_b at SGP. The JD06 retrieval also shows a negative relationship between ϵ and L_{cld}, with a stronger ($R = -0.79$) and significant trend at ENA and a weaker ($R = -0.57$) and not significant trend at SGP (Figs. 4d).

The higher end of L_{cld} values in Fig. 4d (5-10 km) is on the large side for ShCu, which are often characterized by widths of O(1 km) or less. While some large values may be associated with elongated cloud streets, the assumption that clouds propagate with the cloud-bearing layer winds may also tend to overestimate their width. Consideration of velocities from the surface to cloud top, thus encompassing the full boundary-layer circulation supporting the cloud, may be required to more accurately estimate L_{cld}.

Because both z_b and L_{cld} are partially governed by subcloud processes, their relationships with ϵ may reflect more causal sensitivities than those involving cloud-layer vigor. The z_b sensitivity is stronger at ENA ($R = -1$) than at SGP ($R = -0.89$) but is only significant at SGP, while the L_{cld} sensitivity is significant and stronger at ENA. These two parameters are physically linked because the scale of subcloud eddies, and hence the cloud-base width, tends to increase with subcloud-layer depth (Drueke et al. 2020). The negative relationship between ϵ and L_{cld} likely reflects that, by virtue of their larger cross-sectional areas, wider clouds are less diluted by a given entrainment

flux across cloud perimeter. This mechanism apparently overcomes the tendency for entrainment to *widen* clouds by increasing their upward mass flux (Drueke et al. 2020).

In addition, ϵ correlates negatively with cloud-base mass flux, both for individual clouds and cloud ensembles (M_b in Fig. 4e and m_b in Fig. 5d, respectively). Although the M_b correlation is not significant and relatively weak ($R = -0.62$) in the JD06 retrieval at SGP, the consistent negative trend in both retrievals, and at both locations, may indicate physically meaningful relationships. Because these trends largely depend on subcloud, rather than cloud-layer, forcing, they may have a more causal impact on ϵ than cloud-layer parameters. While the negative trend in the D19 retrieval follows from the inverse sensitivity of ϵ_{D19} to $m_b^{2/3}$ in (3), the negative ϵ–M_b trend for individual clouds is novel and less obvious. We speculate that it relates to a transition from more thermal-like to more plume-like cloud circulations, the latter corresponding to stronger and more sustained subcloud updrafts, as M_b increases. Such sustained subcloud inflow may induce less dilution than that in thermal-like updrafts that detach from the subcloud layer (e.g., Squires and Turner 1962).

5. Discussion

a. On the role of continentality

Although several parameters appear to be important for regulating bulk entrainment, not all of these are relevant to the robust land–ocean ϵ contrast in Fig. 1. To help identify the key parameters underlying this contrast, we present climatological distributions of relevant environmental and cloud-related parameters for the JD06 (Figs. 6 and 8) and D19 (Figs. 7 and 9) climatologies, over similar parameter ranges as those shown in the sensitivity analyses of Figs. 2-5.

Notable climatological environmental differences between SGP and ENA include larger $\left(\sigma_w^2\right)_{\mathrm{sc}}$ and smaller $\mathrm{RH}_{\mathrm{cld}}$ at SGP (Figs. 6 and 7), and notable cloud-related differences include larger z_b,

d_{cld}, $w_{\max}$, and cloud-base mass fluxes at SGP (Figs. 8 and 9). Of these parameters, $\mathrm{RH}_{\mathrm{cld}}$, m_b and M_b, and d_{cld} may be expected to be the most important for regulating cloud-layer ϵ (as discussed in section 4b). All of the climatological differences in these four parameters favor larger ϵ at ENA, including its moister and shallower cloud layers and its smaller cloud-base mass fluxes.

To our knowledge, the only other study to hypothesize a mechanism for the land–ocean contrast was Drueke et al. (2020), who argued that increased H over land enhances subcloud turbulence, which increases m_b and thus decreases ϵ via (3). While the land–ocean contrast in ϵ_{D19} may indeed stem in part from increased m_b at SGP (Figs. 8f and 9f), the climatological distributions of H are very similar at SGP and ENA (Figs. 6e and 7e), which, at face value, appears to contradict the hypothesis of Drueke et al. (2020).

The above contradiction may stem from the ENA flux measurements being taken on land, which helps to explain the similarity of the H distributions at SGP and ENA. However, like m_b itself, $\left(\sigma_w^2\right)_{\mathrm{sc}}$ is clearly larger at SGP than at ENA (Figs. 6g and 7g), suggesting much stronger subcloud turbulence at the continental location. To explain this difference, we consider the Deardorff velocity

$$w^* = \left(\frac{g}{T_v} z_i \overline{w'\theta_v'}\right)^{1/3}, \tag{4}$$

where $z_i \approx z_b$ is the mixed-layer depth and $\overline{w'\theta_v'}$ is the surface buoyancy flux. With the aid of Figs. 7f and 9a, we estimate characteristic values of the above parameters at ENA ($T_v = 290$ K, $z_i = 1$ km, $\rho_s c_p \overline{w'\theta_v'} \approx H = 200$ W m^{-2}, where $\rho_s = 1.2$ kg m^{-3} is surface density and c_p is the specific heat of dry air), and obtain $w^* = 1.7$ m s^{-1} and an eddy turnover time of $\tau_{\mathrm{eddy}} = z_i/w^* = 565$ s. Assuming $V_{\mathrm{sc}} = 10$ m s^{-1} (Fig. 6e), an onshore fetch of 5.6 km would be required to complete a single eddy turnover. Given that ENA is < 1 km from the nearest coastline to its north, and the entire island area is only about 60 km^2, many ENA flows may indeed lack sufficient time to adjust to the increased H over land.

To probe the above argument more deeply, we examine the relationships between H, $\left(\sigma_w^2\right)_{\rm sc}$, and m_b for the D19 climatology. Although H and $\left(\sigma_w^2\right)_{\rm sc}$ are positively correlated at both sites, the trend is stronger at SGP (Fig. 10a), particularly for the majority of cases for which $H < 300$ W m^{-2} (Fig. 7f). This difference implies that the local turbulence spinup issue is much more of a factor at ENA than at SGP. The small values of $\left(\sigma_w^2\right)_{\rm sc}$ at ENA, and their relative insensitivity to H, reinforce the notion of under-developed turbulence over the small island. Given the strong positive correlation between $\left(\sigma_w^2\right)_{\rm sc}$ and m_b in Fig. 10b, the smaller $\left(\sigma_w^2\right)_{\rm sc}$ at ENA implies smaller m_b and, as a result, larger ϵ via (3). Thus, despite the similarities in H at SGP and ENA, the large impact of m_b on the land–ocean ϵ contrast hypothesized by Drueke et al. (2020) still appears to hold.

b. Directions for improvement

Both bulk retrievals contain assumptions that may impact the accuracy of the ϵ climatologies. Furthermore, cloud radar information is only obtained through cloud chords, which do not necessarily represent the cloud entity as a whole. Our use of two retrievals helps to overcome these limitations by identifying some robust trends common to both climatologies, and our sampling of many clouds over a long time period helps to obtain meaningful correlations despite a large degree of spread. However, a more attractive approach would be to develop a single ShCu ϵ retrieval with less uncertainty than the ones considered herein. The method of Wagner et al. (2013) is one such candidate, but it was found to be much less accurate than the D19 or JD06 methods in the numerical verification exercise of D19. Moreover, this method is very computationally demanding, which makes it impractical for climatologies over several thousands of clouds.

One potential area of improvement would be to account for the effects of vertical wind shear in the D19 retrieval. Although neither climatology indicated a strong sensitivity of ϵ to $S_{\rm cld}$, recent LES experiments suggest a positive sensitivity, at least in oceanic ShCu (Drueke et al. 2019a). For

D19 to potentially capture this effect, the shear production term must be retained in the TKE budget, and the budget must be rescaled accordingly. Moreover, the JD06 retrieval would benefit from additional thermodynamic information to better constrain ϵ. If in-cloud or cloud-top temperatures were available from MWRs, satellites, or aircraft, these could be used to relax the zero cloud-top buoyancy assumption. Furthermore, more realistic (and likely stochastic) entraining parcel models (e.g., Romps 2016) could replace the simplified model used in JD06.

Our analysis may also suffer from the fact that it is based on point observations and thus does not capture clouds as a whole or the path they covered over their life cycle. A more comprehensive 3D view of clouds could be achieved using scanning cloud radar observations guided by frameworks such as the Multisensor Agile Adaptive Sampling (MAAS; Kollias et al. 2020) or alternatively by cloud stereogrammatic techniques (e.g., Romps and Öktem 2019). As for surface fluxes, observations from multiple surface-flux instruments deployed in a mesoscale network, or complementing the observations with reanalysis data, would be superior to single point measurements.

6. Conclusions

This study has generated climatologies of retrieved bulk entrainment (ϵ) in active, fair-weather shallow cumuli (ShCu) at two Department of Energy (DoE) Atmospheric Radiation Measurement (ARM) observatories, the continental Southern Great Plains site (SGP; south-central US) and oceanic Eastern North Atlantic site (ENA; Azores islands). Two ground-based ϵ retrievals are deployed, one applying to individual cumuli and the other applying to cumulus ensembles. The former uses an entraining parcel model to match the parcel entraining level of neutral buoyancy to the radar-observed cloud top (Jensen and Del Genio 2006, or JD06) and the latter uses an analytical formulation based on a scaling of the equilibrium TKE budget (Drueke et al. 2019b, or D19). The

climatologies cover an equivalent, roughly 4-year period (October 2015 to December 2019) and are limited to daytime, surface-based, and active (buoyant) cumuli. Altogether, 175 (631) cloud ensembles and 887 (3,724) individual clouds are analyzed at SGP (ENA).

While each retrieval makes important assumptions about highly complex cloud processes, the use of two independent methods helps to identify robust sensitivities of ϵ in the face of such uncertainties. The two retrievals yield consistent magnitudes of ϵ at both sites as well as a large degree of consistency in the various environmental and cloud-related sensitivities of ϵ. This consistency implies that the simple formula used for cloud-ensemble ϵ in the D19 method may be applied to aid physical interpretation. In this formula (shown in equation (3)), ϵ depends directly on $\mathrm{CAPE}^{1/3}$ and inversely on cloud-base mass flux ($m_b^{2/3}$) and cloud-layer depth (d_{cld}).

Certain correlations between the retrieved ϵ and environmental and cloud-related parameters are consistent with previously reported experimental trends. A strong positive correlation with cloud-layer relative humidity was found, which may stem from the tendency of cloud-environmental mixtures in drier layers to undergo buoyancy reversal and detrain rather than entrain (e.g., Drueke et al. 2020). Also, a negative relationship between ϵ and cloud width (L_{cld}) reinforces that wider clouds are prone to less dilution than narrower clouds (e.g., Rousseau-Rizzi et al. 2017). The retrieved ϵ also correlated negatively with measures of cloud-related vigor (e.g., cloud depth and maximum vertical velocity), but these should be interpreted with caution because these parameters may depend on ϵ more than they exert control over it.

Some novel sensitivities of ϵ were also found, one being a robust decrease with increasing subcloud winds at the oceanic ENA site. This trend may stem from the tendency for cumuli to deepen in stronger oceanic flows (Nuijens and Stevens 2012), combined with the tendency of ϵ to vary inversely with cloud-layer depth. Secondly, the D19- and JD06-retrieved ϵ varied inversely with ensemble (m_b) and individual-cloud (M_b) cloud-base mass fluxes, respectively. The former

trend is consistent with the underlying TKE similarity theory (Grant and Brown 1999), but the latter is novel and merits explanation. While it may simply relate to the aforementioned sensitivity of retrieved ϵ to L_{cld}, it may also reflect a transition from ephemeral subcloud thermals to more sustained, plume-like, and less diluted updrafts as M_b increases.

Another key finding was a strong land–ocean contrast in retrieved ϵ, with median values nearly doubling from 0.5-0.6 km^{-1} at the continental SGP site to 1.0-1.1 km^{-1} at the oceanic ENA site. This sharp contrast is consistent with corresponding trends found in large-eddy simulations (Drueke et al. 2020). It is associated with several environmental and cloud-related parameters that all favor smaller ϵ over land, including larger cloud-base mass fluxes and deeper and drier cloud layers.

The trends in retrieved bulk entrainment identified herein may be useful for improving cumulus parameterization schemes. For example, the strong positive sensitivity to cloud-layer relative humidity found herein contrasts with the negative sensitivity incorporated in the parameterization of Bechtold et al. (2008). Such discrepancies merit resolution, which may lead to an improved parameterization of interactions between updraft plumes and their environment. The sensitivity of ϵ to continentality, and to low-level winds over the oceans, may also warrant inclusion in these parameterizations. Similar land–ocean ϵ contrasts have been included in certain parameterization schemes (e.g., Zhao et al. 2009; McTaggart-Cowan et al. 2019), mainly as a tuning exercise to improve model skill. The current results provide empirical support for such contrasts.

Finally, we caution that the effort to retrieve ϵ is still in its infancy. Both of the ϵ retrievals used in this study are highly simplified and could be improved by adding additional observational constraints to relax certain assumptions. Future work will aim to improve these retrievals accordingly, as well as to design numerical experiments to help interpret statistical relationships between ϵ and various environmental and cloud-related parameters.

Acknowledgments. This research was supported by the U.S. Department of Energy's Atmospheric System Research, an Office of Science Biological and Environmental Research program, under grant DE-SC0020083. K. Lamer's contributions were supported by Brookhaven National Laboratory LDRD #20-002 EE/EBNN. The authors are grateful for constructive discussions with Pavlos Kollias over the course of this work, as well as the constructive comments of three anonymous reviewers.

Data availability statement. All of the data used for the present analysis was downloaded from the ARM website (https://www.arm.gov/data) and is freely available to interested researchers. Codes written for data analysis and intermediate data products are all archived locally and available upon request to the corresponding author.

APPENDIX

References

Battaglia, A., P. Kollias, R. Dhillon, K. Lamer, M. Khairoutdinov, and D. Watters, 2020: Mind the gap–part 2: Improving quantitative estimates of cloud and rain water path in oceanic warm rain using spaceborne radars. *Atmos. Meas. Tech.*, **13 (9)**, 4865–4883, doi:10.5194/amt-13-4865-2020, URL https://amt.copernicus.org/articles/13/4865/2020/.

Bechtold, P., M. KÃűhler, T. Jung, F. Doblas-Reyes, M. Leutbecher, M. J. Rodwell, F. Vitart, and G. Balsamo, 2008: Advances in simulating atmospheric variability with the ECMWF model: From synoptic to decadal time-scales. *Quart. J. Roy. Meteor. Soc.*, **134 (634)**, 1337–1351, doi:10.1002/qj.289.

Bera, S., and T. V. Prabha, 2019: Parameterization of entrainment rate and mass flux in continental cumulus clouds: Inference from large eddy simulation. *J. Geophys. Res.-Atmos.*, **124 (23)**, 13 127–13 139, doi:10.1029/2019JD031078.

Betts, A. K., 1975: Parametric interpretation of trade-wind cumulus budget studies. *J. Atmos. Sci.*, **32 (10)**, 1934–1945, doi:10.1175/1520-0469(1975)032<1934:PIOTWC>2.0.CO;2.

Bony, S., and J.-L. Dufresne, 2005: Marine boundary layer clouds at the heart of tropical cloud feedback uncertainties in climate models. *Geophys. Res. Lett.*, **32 (20)**, doi:10.1029/2005GL023851.

Brown, A. R., 1999: The sensitivity of large-eddy simulations of shallow cumulus convection to resolution and subgrid model. *Quart. J. Roy. Meteor. Soc.*, **125**, 469–482.

Brown, A. R., and Coauthors, 2002: Large-eddy simulation of the diurnal cycle of shallow cumulus convection over land. *Quart. J. Roy. Meteor. Soc.*, **128 (582)**, 1075–1093, doi:10.1256/003590002320373210.

Dawe, J. T., and P. H. Austin, 2011: Interpolation of LES cloud surfaces for use in direct calculations of entrainment and detrainment. *Mon. Wea. Rev.*, **139 (2)**, 444–456, doi: 10.1175/2010MWR3473.1.

Del Genio, A. D., and J. Wu, 2010: The role of entrainment in the diurnal cycle of continental convection. *J. Climate*, **23 (10)**, 2722–2738, doi:10.1175/2009JCLI3340.1.

Dirmeyer, P. A., and Coauthors, 2012: Simulating the diurnal cycle of rainfall in global climate models: resolution versus parameterization. *Clim. Dyn.*, **39 (1)**, 399–418.

Drueke, S., D. J. Kirshbaum, and P. Kollias, 2019a: Cumulus entrainment: Verifying retrieval methods and interpreting environmental sensitivities using large-eddy simulation, URL https://ams.confex.com/ams/15CLOUD15ATRAD/webprogram/Paper347394.html, American Meteorological Society 15th Conference on Cloud Physics.

Drueke, S., D. J. Kirshbaum, and P. Kollias, 2019b: Evaluation of shallow-cumulus entrainment rate retrievals using large-eddy simulation. *J. Geophys. Res.-Atmos.*, **124 (16)**, 9624–9643, doi:10.1029/2019JD030889.

Drueke, S., D. J. Kirshbaum, and P. Kollias, 2020: Environmental sensitivities of shallow-cumulus dilution. Part I: Selected thermodynamic conditions. *Atmos. Chem. Phys.*, doi: 10.5194/acp-2020-336, in press.

Gerber, H., G. Frick, J. B. Jensen, and J. Hudson, 2008: Entrainment, mixing, and microphysics in trade-wind cumulus. *J. Meteor. Soc. Japan*, **86**, 87–106.

Grant, A. L. M., and A. R. Brown, 1999: A similarity hypothesis for shallow-cumulus transports. *Quart. J. Roy. Meteor. Soc.*, **125**, 1913–1936.

Grant, A. L. M., and A. P. Lock, 2004: The turbulent kinetic energy budget for shallow cumulus convection. *Quart. J. Roy. Meteor. Soc.*, **130**, 401–422.

Gregory, D., 2001: Estimation of entrainment rate in simple models of convective clouds. *Quart. J. Roy. Meteor. Soc.*, **127 (571)**, 53–72, doi:10.1002/qj.49712757104.

Heymsfield, A. J., P. N. Johnson, and J. E. Dye, 1978: Observations of moist adiabatic ascent in northeast Colorado cumulus congestus clouds. *J. Atmos. Sci.*, **35 (9)**, 1689–1703, doi:10.1175/1520-0469(1978)035<1689:OOMAAI>2.0.CO;2.

Jensen, M. P., and A. D. Del Genio, 2006: Factors limiting convective cloud-top height at the ARM Nauru Island Climate Research Facility. *J. Climate*, **19 (10)**, 2105–2117, doi:10.1175/JCLI3722.1.

Khairoutdinov, M., and D. Randall, 2006: High-resolution simulation of shallow-to-deep convection transition over land. *J. Atmos. Sci.*, **63**, 3421–3436.

Kirshbaum, D. J., and A. L. M. Grant, 2012: Invigoration of cumulus cloud fields by mesoscale ascent. *Quart. J. Roy. Meteor. Soc.*, **138**, 2136–2150.

Klocke, D., R. Pincus, and J. Quaas, 2011: On constraining estimates of climate sensitivity with present-day observations through model weighting. *J. Climate*, **24 (23)**, 6092–6099, doi:10.1175/2011JCLI4193.1.

Kollias, P., E. Luke, M. Oue, and K. Lamer, 2020: Agile adaptive radar sampling of fast-evolving atmospheric phenomena guided by satellite imagery and surface cameras. *Geophys. Res. Lett.*, **47 (14)**, e2020GL088 440, doi:https://doi.org/10.1029/2020GL088440, e2020GL088440 2020GL088440.

Lamer, K., and P. Kollias, 2015: Observations of fair-weather cumuli over land: Dynamical factors controlling cloud size and cover. *Geophys. Res. Lett.*, **42 (20)**, 8693–8701, doi:10.1002/2015GL064534.

Lamer, K., P. Kollias, and L. Nuijens, 2015: Observations of the variability of shallow trade wind cumulus cloudiness and mass flux. *Journal of Geophysical Research: Atmospheres*, **120 (12)**, 6161–6178, doi:https://doi.org/10.1002/2014JD022950.

Lasher-trapp, S. G., W. A. Cooper, and A. M. Blyth, 2005: Broadening of droplet size distributions from entrainment and mixing in a cumulus cloud. *Quart. J. Roy. Meteor. Soc.*, **131 (605)**, 195–220, doi:10.1256/qj.03.199.

Lu, C., and Coauthors, 2018: Observational relationship between entrainment rate and environmental relative humidity and implications for convection parameterization. *Geophys. Res. Lett.*, **45 (24)**, 13,495–13,504, doi:https://doi.org/10.1029/2018GL080264.

Luo, Z. J., G. Y. Liu, and G. L. Stephens, 2010: Use of A-Train data to estimate convective buoyancy and entrainment rate. *Geophys. Res. Lett.*, **37 (9)**, doi:10.1029/2010GL042904.

Markowski, P., and Y. Richardson, 2010: *Mesoscale Meteorology in Midlatitudes*. Wiley, 430 pp.

McCarthy, J., 1974: Field verification of the relationship between entrainment rate and cumulus cloud diameter. *J. Atmos. Sci.*, **31 (4)**, 1028–1039, doi:10.1175/1520-0469(1974)031<1028:FVOTRB>2.0.CO;2.

McTaggart-Cowan, R., P. A. Vaillancourt, A. Zadra, L. Separovic, S. Corvec, and D. Kirshbaum, 2019: A lagrangian perspective on parameterizing deep convection. *Mon. Wea. Rev.*, **147 (11)**, 4127 – 4149, doi:10.1175/MWR-D-19-0164.1.

679 Neggers, R. A. J., A. P. Siebesma, and H. J. J. Jonker, 2002: A multiparcel model for shallow cu-
680 mulus convection. *J. Atmos. Sci.*, **59 (10)**, 1655–1668, doi:10.1175/1520-0469(2002)059<1655:
681 AMMFSC>2.0.CO;2.

682 Nuijens, L., and B. Stevens, 2012: The influence of wind speed on shallow marine cumulus
683 convection. *J. Atmos. Sci.*, **69 (1)**, 168–184, doi:10.1175/JAS-D-11-02.1.

684 Peters, J. M., C. J. Nowotarski, and H. Morrison, 2019: The role of vertical wind shear in
685 modulating maximum supercell updraft velocities. *J. Atmos. Sci.*, **76 (10)**, 3169–3189, doi:
686 10.1175/JAS-D-19-0096.1.

687 Raga, G. B., J. B. Jensen, and M. B. Baker, 1989: Characteristics of cumulus band clouds off
688 the coast of Hawaii. *J. Atmos. Sci.*, **47 (3)**, 338–356, doi:10.1175/1520-0469(1990)047<0338:
689 COCBCO>2.0.CO;2.

690 Rieck, M., C. Hohenegger, and C. C. van Heerwaarden, 2014: The influence of land surface
691 heterogeneities on cloud size development. *Mon. Wea. Rev.*, **142 (10)**, 3830–3846, doi:10.1175/
692 MWR-D-13-00354.1.

693 Romps, D. M., 2010: A direct measure of entrainment. *J. Atmos. Sci.*, **67 (6)**, 1908–1927, doi:
694 10.1175/2010JAS3371.1.

695 Romps, D. M., 2016: The Stochastic Parcel Model: A deterministic parameterization of stochas-
696 tically entraining convection. *J. Adv. Model. Earth Sy.*, **8 (1)**, 319–344.

697 Romps, D. M., and R. Öktem, 2019: Observing clouds in 4d with multiview stereophotogrammetry.
698 *Bull. Amer. Meteor. Soc.*, **99 (12)**, 2575–2586, doi:10.1175/BAMS-D-18-0029.1.

Rougier, J., D. M. H. Sexton, J. M. Murphy, and D. Stainforth, 2009: Analyzing the climate sensitivity of the HadSM3 climate model using ensembles from different but related experiments. *J. Climate*, **22 (13)**, 3540–3557, doi:10.1175/2008JCLI2533.1.

Rousseau-Rizzi, R., D. J. Kirshbaum, and M. K. Yau, 2017: Initiation of deep convection over an idealized mesoscale convergence line. *J. Atmos. Sci.*, **74 (3)**, 835–853, doi:10.1175/JAS-D-16-0221.1.

Siebesma, A. P., and J. W. M. Cuijpers, 1995: Evaluation of parametric assumptions for shallow cumulus convection. *J. Atmos. Sci.*, **52 (6)**, 650–666, doi:10.1175/1520-0469(1995)052<0650:EOPAFS>2.0.CO;2.

Siebesma, A. P., and Coauthors, 2003: A large eddy intercomparison study of shallow cumulus convection. *J. Atmos. Sci.*, **60**, 1201–1219.

Squires, P., and J. S. Turner, 1962: An entraining jet model for cumulo-nimbus updraughts. *Tellus*, **14 (4)**, 422–434, doi:10.3402/tellusa.v14i4.9569.

Stirling, A. J., and R. A. Stratton, 2012: Entrainment processes in the diurnal cycle of deep convection over land. *Quart. J. Roy. Meteor. Soc.*, **138 (666)**, 1135–1149, doi:10.1002/qj.1868.

Takahashi, H., Z. J. Luo, and G. L. Stephens, 2017: Level of neutral buoyancy, deep convective outflow, and convective core: New perspectives based on five years of CloudSat data. *J. Geophys. Res.-Atmos.*, **122 (5)**, 2958–2969, doi:10.1002/2016JD025969.

Tian, Y., and Z. Kuang, 2016: Dependence of entrainment in shallow cumulus convection on vertical velocity and distance to cloud edge. *Geophys. Res. Lett.*, **43 (8)**, 4056–4065, doi:10.1002/2016GL069005.

Wagner, T. J., D. D. Turner, L. K. Berg, and S. K. Krueger, 2013: Ground-based remote retrievals of cumulus entrainment rates. *J. Atmos. Ocean. Tech.*, **30 (7)**, 1460–1471, doi: 10.1175/JTECH-D-12-00187.1.

Yamaguchi, T., G. Feingold, and J. Kazil, 2019: Aerosol-cloud interactions in trade wind cumulus clouds and the role of vertical wind shear. *J. Geophys. Res.-Atmos.*, **124 (22)**, 12 244–12 261, doi:https://doi.org/10.1029/2019JD031073.

Zhang, G. J., X. Wu, X. Zeng, and T. Mitovski, 2016: Estimation of convective entrainment properties from a cloud-resolving model simulation during TWP-ICE. *Clim. Dyn.*, **47**, 2177–2192, doi:10.1007/s00382-015-2957-7.

Zhang, Y., and S. A. Klein, 2010: Mechanisms affecting the transition from shallow to deep convection over land: Inferences from observations of the diurnal cycle collected at the ARM Southern Great Plains site. *J. Atmos. Sci.*, **67 (9)**, 2943–2959, doi:10.1175/2010JAS3366.1.

Zhao, M., I. M. Held, S.-J. Lin, and G. A. Vecchi, 2009: Simulations of global hurricane climatology, interannual variability, and response to global warming using a 50-km resolution GCM. *J. Climate*, **22 (24)**, 6653 – 6678, doi:10.1175/2009JCLI3049.1.

LIST OF TABLES

TABLE 1: List of mathematical symbols and abbreviations used in the text.

Symbol	Definition	Symbol	Definition
ϵ	Fractional bulk entrainment rate	E	Bulk entrainment rate
ϵ_{JD06}	ϵ from JD06 retrieval	ϵ_{D19}	ϵ from the D19 retrieval
A_ϵ	Fraction of buoyancy production available for entrainment	θ_e	Equivalent potential temperature
T_v	Virtual temperature	θ_v	Virtual potential temperature
ρ_b	Cloud-base air density	ρ_s	Surface air density
t_{up}	Time-duration of cloud-base updraft	f_{up}	Fraction of cloud-base points undergoing ascent
w_{up}	Mean ascent rate of cloud-base updraft	L_{up}	Width of cloud-base updraft
w	Vertical velocity	b	Buoyancy
z_b	Cloud-base height	z_t	Cloud-top height
g	Gravitational acceleration	z_i	Mixed-layer depth
w^*	Deardorff velocity	τ_{eddy}	Eddy turnover time
LCL	Lifting condensation layer	LFC	Level of free convection
(E)LNB	(Entraining) level of neutral buoyancy	CIN	Convective inhibition
CAPE	Full convective available potential energy	$\mathrm{CAPE}_{\mathrm{cld}}$	Cloud-layer convective available potential energy
m_b	Cloud-base mass flux for cloud ensemble	M_b	Cloud-base mass flux for individual cloud
M_c	Cloud upward mass flux	H	Sensible heat flux
t_{cld}	Cloud duration	$\mathrm{RH}_{\mathrm{cld}}$	Cloud-layer-averaged relative humidity
d_{cld}	Cloud or cloud-layer depth	L_{cld}	Cloud width
S_{cld}	Magnitude of cloud-layer-averaged vertical shear	V_{cld}	Magnitude of cloud-layer-averaged horizontal wind
V_{sc}	Magnitude of subcloud-layer-averaged horizontal wind	$\left(\sigma_w^2\right)_{\mathrm{sc}}$	Subcloud w variance
w_{max}	Maximum in-cloud updraft speed	$\mathrm{LWP}_{\mathrm{max}}$	Maximum cloud liquid-water path
$\mathrm{CCF}_{\mathrm{rad}}$	Cloud-cover fraction for cumulus ensemble	TKE	Turbulent kinetic energy
γ	Doppler Lidar attenuated backscatter	R	Spearman correlation coefficient

LIST OF FIGURES

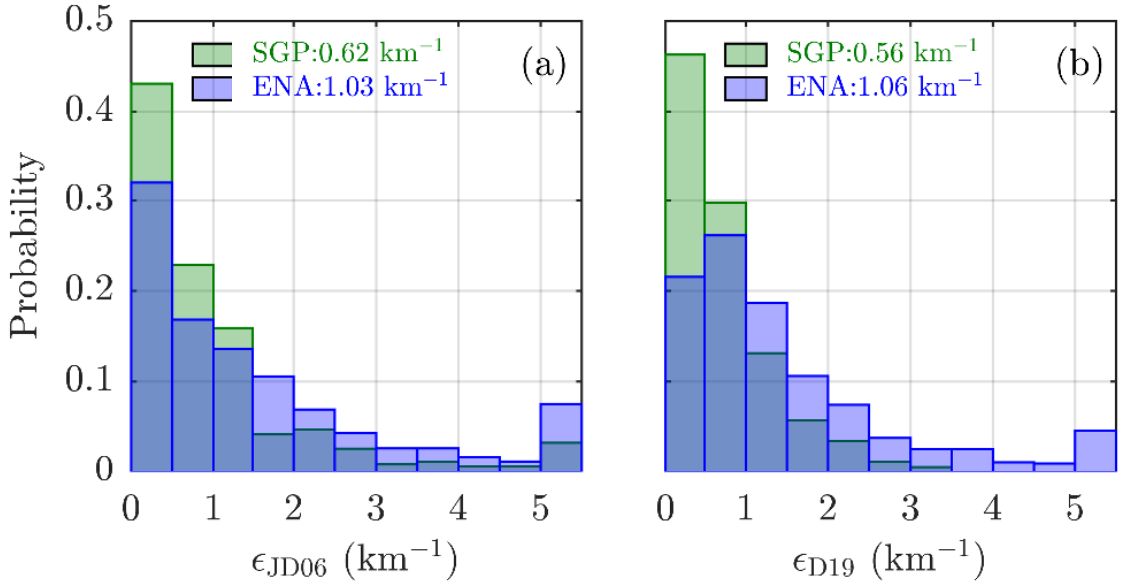

FIG. 1: Histograms of retrieved bulk entrainment using the (a) JD06 and (b) D19 methods. All quantities are defined in the text. The mean values of the distributions are shown in the plot annotation. For both panels, the null hypothesis of equal sample means for JDG and D19 is rejected at the 95% confidence interval using the two-sample t-test.

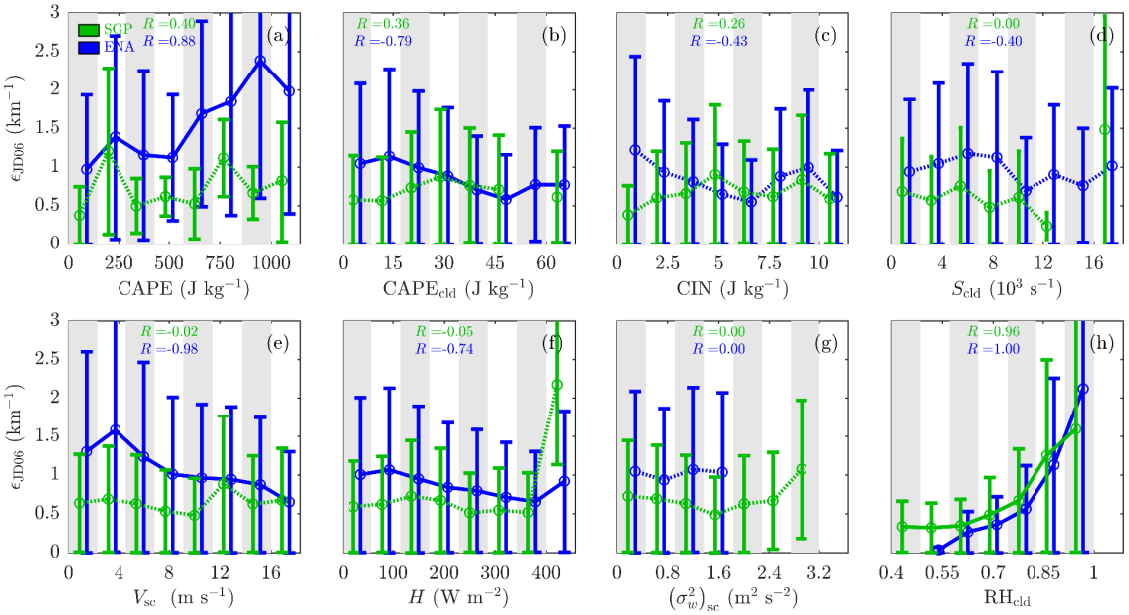

FIG. 2: Sensitivity of JD06-retrieved ϵ (ϵ_{JD06}) to selected environmental parameters. Six bins are defined for each parameter, the first five spanning the range of values shown on the abscissa and the sixth extending from the maximum value to infinity. Curves connect the bin medians (the latter denoted by circles), and error bars show the 25th to 75th percentiles within that bin. Solid curves represent correlations with Spearman correlation coefficient p-values below 0.05; dashed lines have p-values above 0.05. The corresponding Spearman R-values are also provided at the top of each panel. Data is only shown for bins containing at least five data points. All abbreviations are defined in the text.

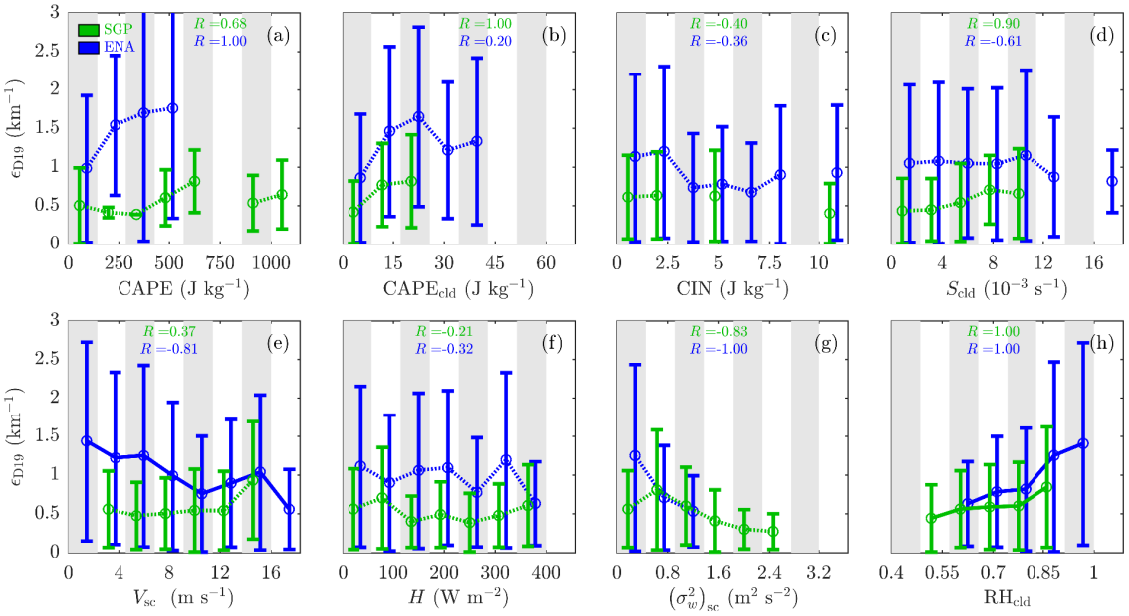

FIG. 3: As in Fig. 2, but for the D19 ϵ retrieval (ϵ_{D19}).

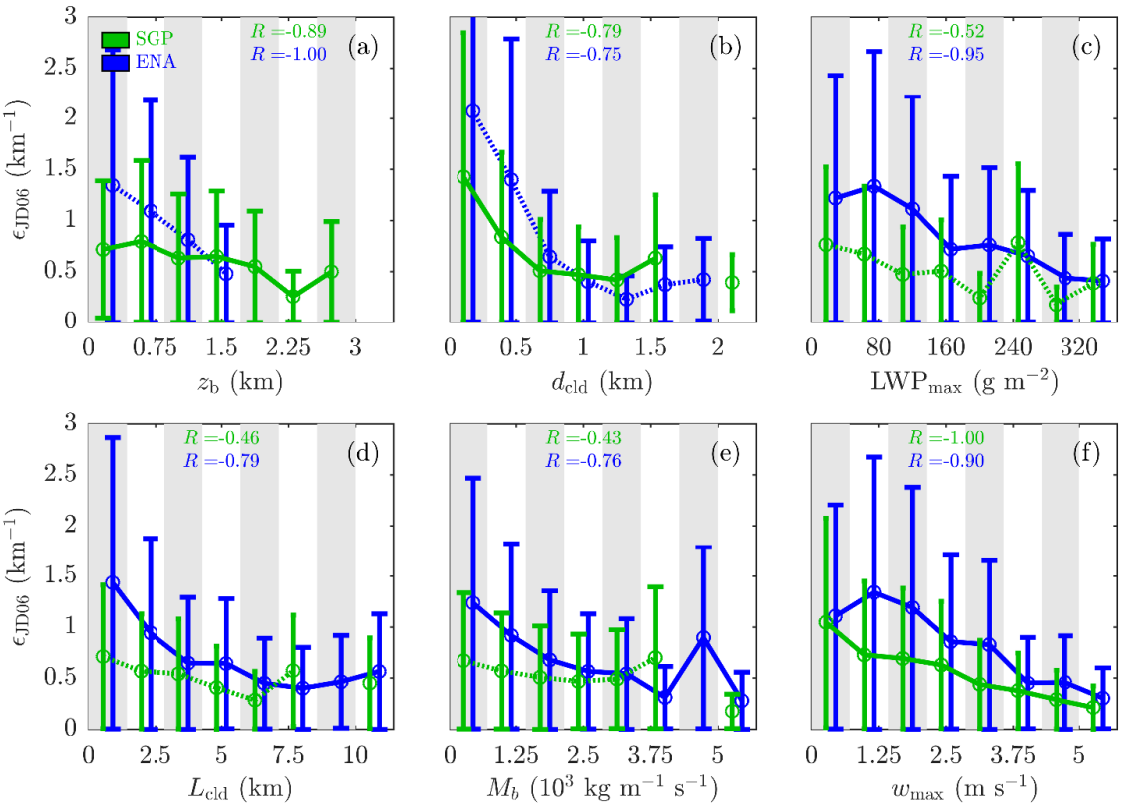

FIG. 4: As in Fig. 2, but for the sensitivity of JD06-retrieved ϵ (ϵ_{JD06}) to selected cloud-related parameters.

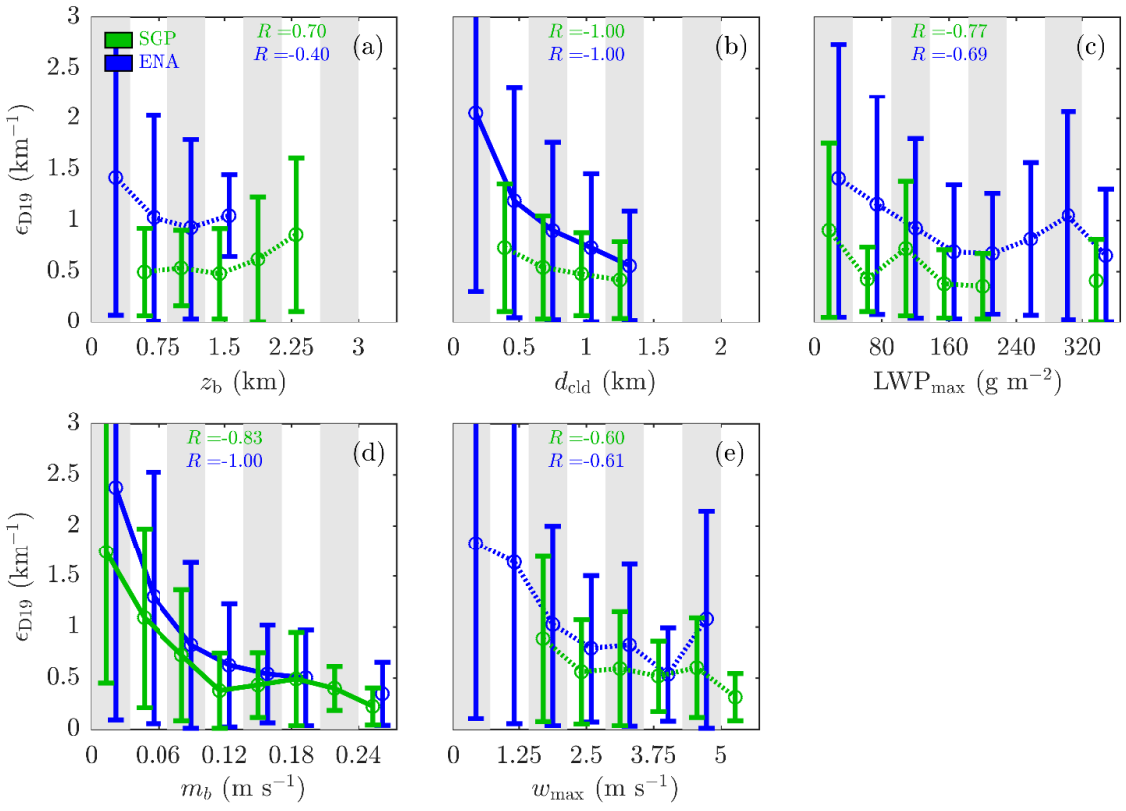

FIG. 5: As in Fig. 3, but for the sensitivity of D19-retrieved ϵ (ϵ_{D19}) to selected cloud-related parameters.

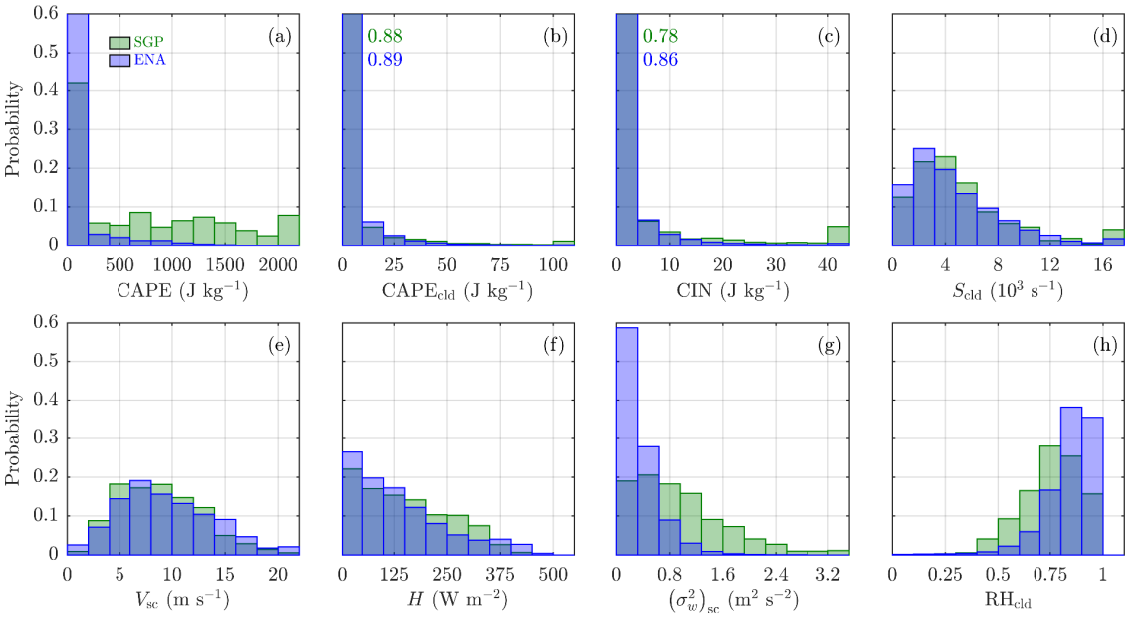

FIG. 6: Histograms of selected environmental parameters at SGP and ENA associated with cumulus ϵ retrievals using the JD06 method. All quantities are defined in the text.

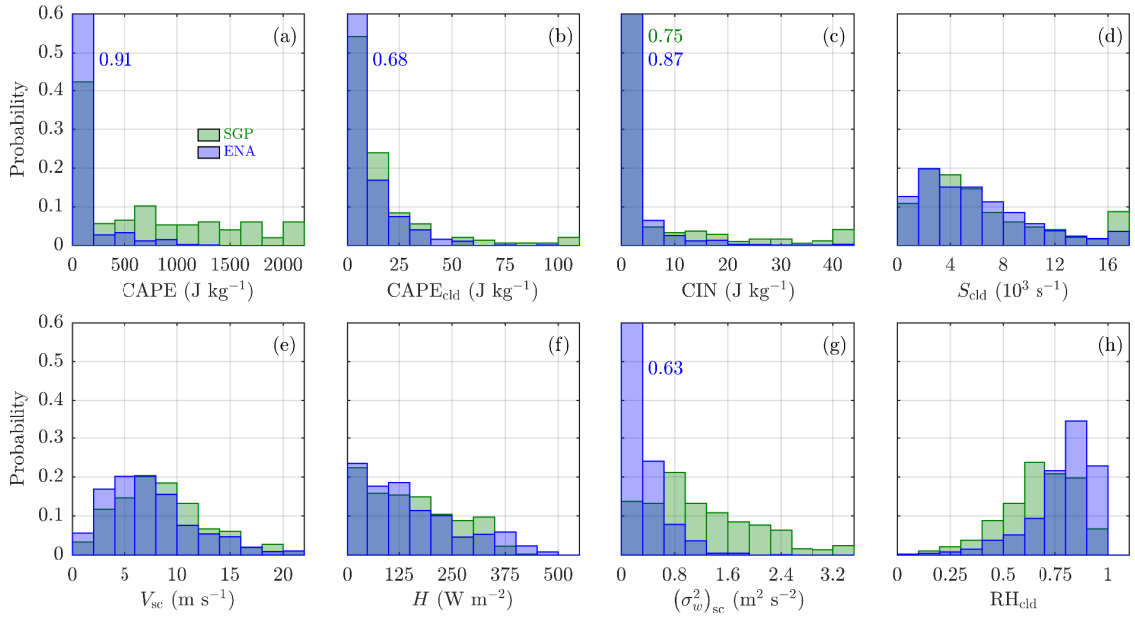

FIG. 7: Histograms of selected environmental parameters at SGP and ENA associated with cumulus ϵ retrievals using the D19 method. All quantities are defined in the text.

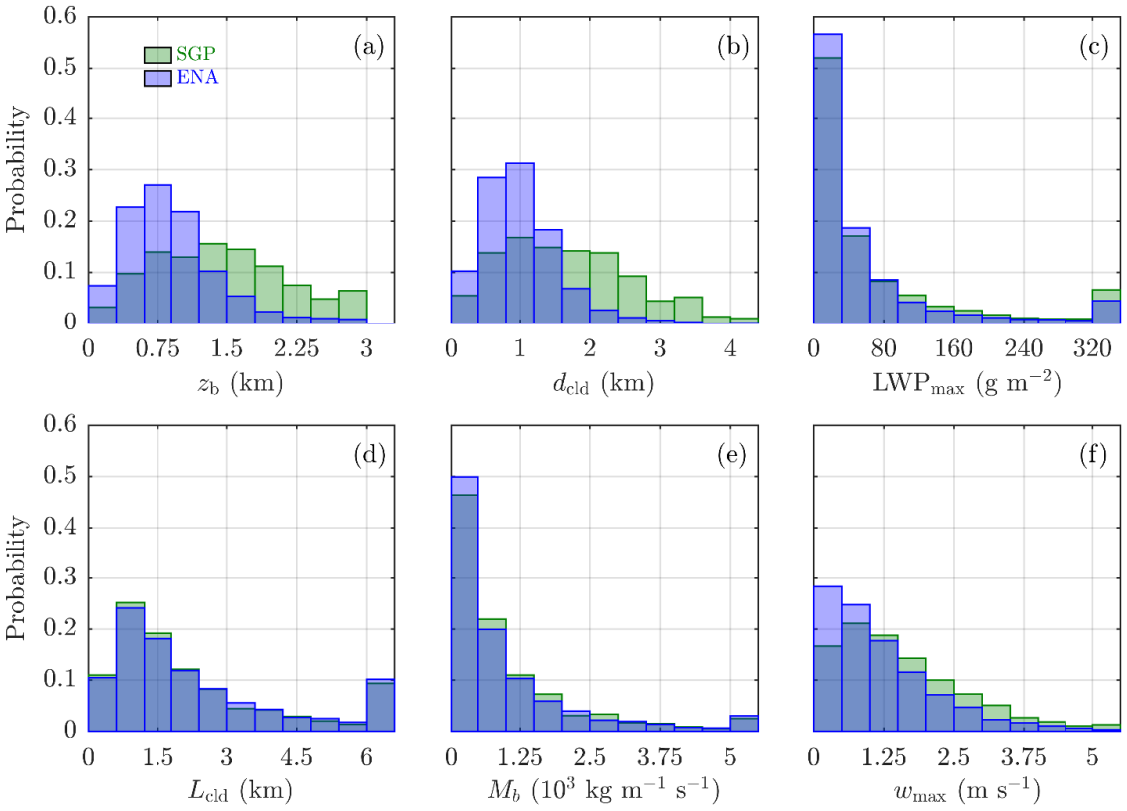

FIG. 8: Histograms of selected cloud-related parameters at SGP and ENA associated with cumulus ϵ retrievals using the JD06 method. All quantities are defined in the text.

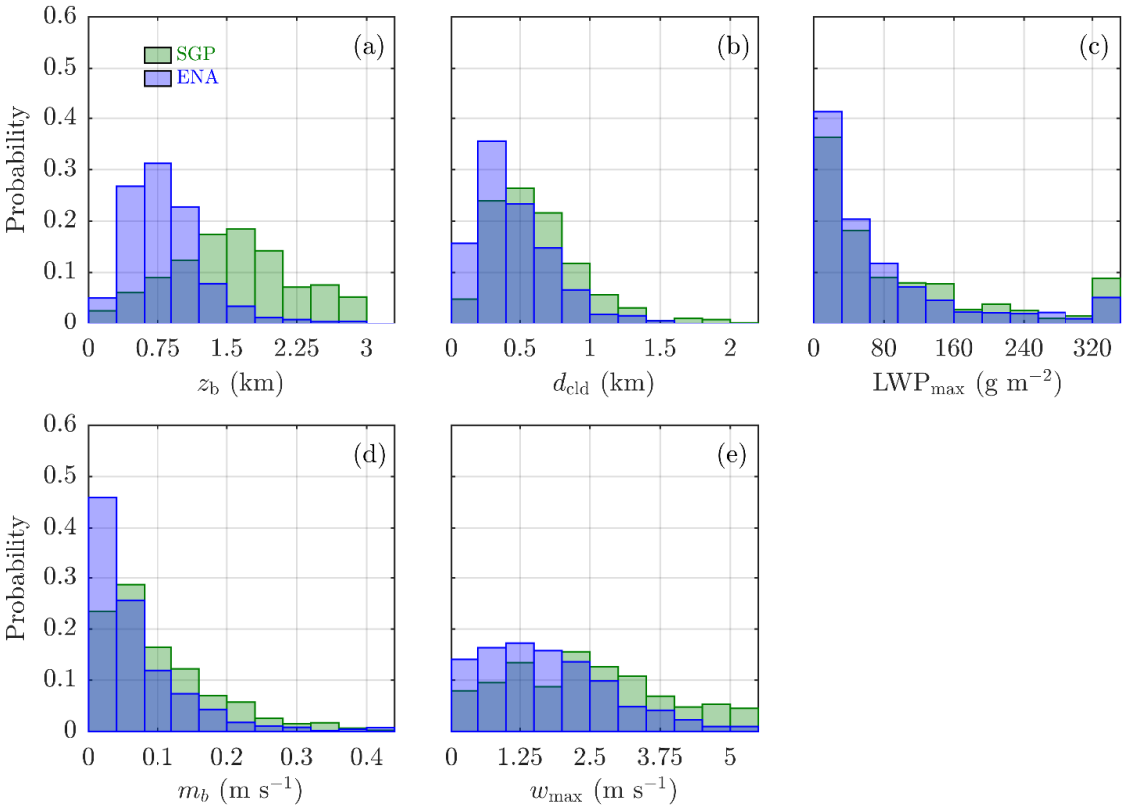

FIG. 9: Histograms of selected cloud-related parameters at SGP and ENA associated with cumulus ϵ retrievals using the D19 method. All quantities are defined in the text.

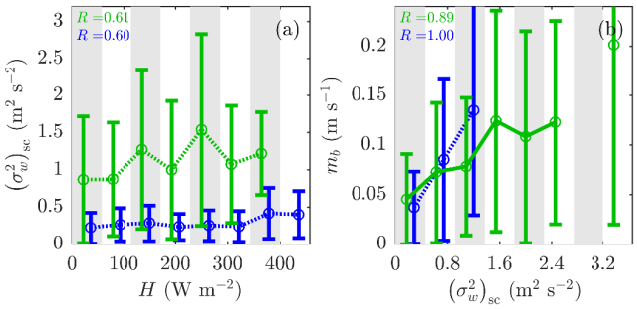

FIG. 10: Evaluation of relationships between different variables of interest. The statistical analysis behind each relationship is identical to that described in Fig. 3.